# CoNiSe₂ heteronanorods decorated with layered-double-hydroxides for efficient hydrogen evolution

Yaqing Yang[a,1], Wenbiao Zhang[a,1], Yongle Xiao[a], Zhangping Shi[b], Xiaoming Cao[c], Yi Tang[b,*], Qingsheng Gao[a,*]

[a] Department of Chemistry, College of Chemistry and Materials Science, Jinan University, Guangzhou 510632, PR China
[b] Department of Chemistry, Shanghai Key Laboratory of Molecular Catalysis and Innovative Materials, Laboratory of Advanced Materials and Collaborative Innovation Center of Chemistry for Energy Materials, Fudan University, Shanghai 200433, China
[c] Centre for Computational Chemistry and Research Institute of Industrial Catalysis, School of Chemistry and Molecular Engineering, East China University of Science & Technology, Shanghai 200237, China

## ARTICLE INFO

## ABSTRACT

Efficient electrocatalysts for hydrogen evolution reaction (HER) are critical to reduce energy losses in alkaline water electrolysis. Herein, CoNiSe₂ heteronanorods decorated with layered-double-hydroxides (LDHs) nanosheets are designed, in which the selenide-LDHs interfaces can boost $H_2O$ chemisorption to produce reactive H intermediate, resulting in fast HER kinetics. Such promotion in HER is further interpreted by theoretical calculation and *in-situ* Raman investigation. By contrast, it's negligible for anodic oxygen evolution. Assembled as an electrolyzer for overall water splitting, the heteronanorods afford a quite low cell voltage of 1.44 V at a geometric current density of $10\,\text{mA}\,\text{cm}^{-2}$ and remarkable stability for more than 48 h in 1.0 M KOH, performing among the best of non-precious electrocatalysts. Identifying efficient electrocatalysis on engineered heterointerfaces, this work is anticipated to open up new opportunities for catalyst design in energy chemistry.

## 1. Introduction

As one of the renewable and clean energy sources, hydrogen is promising to address the rapid growth of global energy consumption and the associated environmental issues [1]. It stores renewable but intermittent electricity sources (e.g., solar and wind) into chemical bonds via water electrolysis, which then can be released via fuel cells on demand [2], thereby averting serious troubles associated with daily/seasonal intermittent and regional variability. In hydrogen evolution reactions (HER) from water electrolysis, electrocatalysts are indispensable to reduce dynamic overpotentials and thus save energy consumption [3]. So far, Pt and its alloys are state-of-the-art electrocatalysts, but are severvly prohibited by the high-cost and scarcity [4]. Tremendous efforts have been devoted to developing noble-metal-free alternatives, such as earth-abundant transition-metals and their chalcogenides, phosphides, carbides, nitrides, etc [5]. Because rare electrocatalysts are stable for oxygen evolution reactions (OER) in acidic media, alkaline HER is more competitive for large-scale $H_2$ production [6]. However, a large part of above electrocatalysts suffer from low activity in alkaline electrolytes, because of the lower kinetics and higher sensitivity to catalyst surface than that in acidic media [7,8]. The key hydrogen intermediate chemisorbed on catalyst surface (denoted as $H_{ads}$) is initiated from discharging $H_2O$ ($H_2O + e^- \rightarrow H_{ads} + OH^-$) in a basic environment [7,9–11], different from the reduction of available hydronium ions in acidic electrolytes ($H_3O^+ + e^- \rightarrow H_{ads} + H_2O$). Thereby, the difficult $H_2O$ discharging serves as the rate-determined step in alkaline HER, requiring efficient electrocatalysts to overcome the energy barrier.

Transition-metal selenides have attracted much attention as non-precious electrocatalysts [12]. They feature several merits [13,14], e.g., outstanding cost-efficiency, low electrical resistivity, high activity over a wide pH range, and bi-functionality for both HER and OER. Intensive efforts have been made to improve the abundance of active-sites by means of constructing one- or two-dimensional (1D or 2D) selenide nanocrystals [15,16], and to optimize the electronic configuration on surface via heteroatom doping or solid-solution phase regulation (e.g., bi- or tri-metallic selenides) [17–20]. In view of the consecutive elementary steps (Volmer-Heyrovsky or Volmer-Tafel) in HER, the rational combination of various catalytic surfaces is of great importance in electrocatalyst design [21,22]. For example, surface/interfacial

---

engineering in selenide-based heterostructures is highly demanded to address the difficult $H_2O$ discharging that produces chemisorbed $H_{ads}$ toward $H_2$ [23]. Wang and co-workers illustrated that $NiO_x$ decoration on $NiSe_2$ nanowires can obviously improve the HER activity in 1.0 M KOH [24]. However, comprehensive interpretation for interfacial synergy was unfortunately absent. Meanwhile, as for bi-functional selenide electrocatalysts, the clear identification on heterointerface effects is further desired for both HER and OER, which will make insight into electrocatalytic mechanism and guide catalyst design.

Regarding strong chemisorption with $H_2O$ molecules on layered-double-hydroxides (LDHs) [25,26], we design free-standing 1D $CoNiSe_2$ surface-decorated by 2D Co-Ni LDHs on nickel foam (denoted as CoNiSe_2@CoNi-LDHs/NF), and investigate the possible promotion by selenides-LDHs heterointerfaces in HER and OER. Remarkably, the optimal LDHs decoration improves the HER activity on CoNiSe_2@CoNi-LDHs heteronanorods. They only requires a low overpotential ($\eta_{10}$) of 106 mV to reach a geometric current density ($j_{geo}$) of $-10$ mA cm$^{-2}$ in 1.0 M KOH, lower than that of CoNiSe_2/NF (192 mV) and CoNi-LDHs/NF (264 mV). The promoted HER on selenide-LDHs interfaces is interpreted by density functional theory (DFT) calculation and *in-situ* Raman analysis. The interfaces enhance $H_2O$ chemisorption and thereby accelerate water dissociation to produce reactive $H_{ads}$, accomplishing the promoted HER kinetics in an alkaline environment. By contrast, such effect is negligible in OER owing to the different reaction pathways. Moreover, the CoNiSe_2@CoNi-LDHs/NF further reveals a superior activity for overall water splitting with a quite low cell voltage of 1.44 V at $j_{geo} = 10$ mA cm$^{-2}$, outperforming most of noble-metal-free materials, and even a benchmarking $IrO_2/C - Pt/C$ couple.

## 2. Experimental details

### 2.1. Catalyst preparation

#### 2.1.1. Synthesis of CoNi-precursor/NF

In order to get rid of surface oxides, commercial NF ($1 \times 5$ cm$^2$) was immersed in acetone for 1 h, and then bleached by 3 M HCl solution for 2 h. The refreshed NF was further transferred into a Teflon-lined stainless steel autoclave containing cobalt nitrate hexahydrate (1.16 g), urea (0.45 g), ethanol (1.7 mL) and deionized water (30.0 mL). After reactions at 120 °C for 4 h, the CoNi-precursor/NF was received.

#### 2.1.2. Synthesis of fresh NaHSe

According to the previous report [27], 0.08 g of $NaBH_4$ was dissolved in 1 mL of deionized water that was statured by $N_2$. And then, 0.08 g of Se powder was added into the above solution. Se powder was completely dissolved as the solution was gently shaken. When the solution turned to atropurpureus, the NaHSe was obtained.

#### 2.1.3. Synthesis of CoNiSe_2/NF

A piece of as-prepared CoNi-precursor/NF was placed into a Teflon-lined stainless steel autoclave, in which 1 M NaHSe solution (1 mL) and deionized water (19 mL) have been already loaded. After treatment at 160 °C for 24 h, the CoNiSe_2/NF was received.

#### 2.1.4. Synthesis of CoNiSe_2@CoNi-LDHs/NF

A standard 3-electrode configuration was employed for electrodeposition. The CoNiSe_2/NF was the working electrode, and a graphite rod and a saturated calomel electrode were the counter and reference electrodes, respectively. The electrolyte was freshly prepared by dissolving 0.15 mol of $Co(NO_3)_2 \cdot 6H_2O$ and 0.15 mol of $Ni(NO_3)_2 \cdot 6H_2O$ into 25 mL of deionized water. After electrodeposition at -1.0 V for varied time, CoNiSe_2@CoNi-LDHs/NF was fabricated. The loading mass of electrocatalysts (selenides and LDHs) on such NF, calculated from the weight increment after catalyst preparation, was approximately 10 mg cm$^{-2}$.

#### 2.1.5. Synthesis of IrO_2/C

According to the previous report [28], 11.4 g of $H_2IrCl_6$ solution (Ir: 0.35 wt%) and 0.19 g of trisodium citrate dehydrate were dissolved in 50 mL of $H_2O$. 1 M NaOH was added to adjust pH to 7.5, and then the solution was heated to 95 °C for 30 min. Afterwards, 0.184 g of carbon black (Vulcan XC72R) was added. The mixture was further refluxed at 95 °C for 2 h in $O_2$ atmosphere, resulting in black solids. To remove organic ligands, the solids were dried at 70 °C in vacuum, and then heated at 300 °C for 30 min in air.

### 2.2. Physical characterization

Scanning electronic microscopy (SEM) and transition electronic microscopy (TEM) were taken on a ZEISS ULTRA55 and JEOL JEM 2100F, respectively. Energy dispersive spectroscopy (EDS) and elemental mapping attached on TEM were conducted on a JEOL JEM 2100F. X-ray diffraction (XRD) patterns were collected on Bruker D8 diffractometer, using Cu Ka radiation ($\lambda = 1.54056$ Å). X-ray photoelectron spectroscopy (XPS) was processed on Thermo scientific Escalab 250Xi, in which C 1 s (284.6 eV) was used as a reference. And Raman spectroscopy was collected on a HORIBA LabRAM HR-800 device, with a laser excitation wavelength of 532 nm.

### 2.3. Electrochemical measurements

The electrochemical measurements of HER and OER were performed in a three-electrode system with an electrochemical workstation (CHI 760, Shanghai Chenhua). The CoNiSe_2@CoNi-LDHs/NF was used as the free-standing working electrode, with a size of 0.5 cm × 0.5 cm, and a graphite rod and saturated calomel electrode were the counter and reference electrode, respectively. As for the Pt/C and $IrO_2/C$, the catalysts were loaded onto NF with the same mass loading. 4 mg of catalysts were dispersed in 1 mL of water/ethanol ($V_{H_2O}/V_{EtOH} = 4$) and 10 μL of 5% PVDF solution by sonication, to form a homogeneous ink, and then loaded onto NF. Linear sweep voltammetry (LSV) for HER and cyclic voltammograms (CVs) for OER were conducted in 1.0 M KOH. Electrochemical impedance spectra (EIS) were measured from $10^{-2}$ to $10^6$ Hz, with an amplitude of 5 mV. For overall water splitting, the CoNiSe_2@CoNi-LDHs/NF was integrated as both anode and cathode in a two-electrode cell. And the potentials reported in this work were referenced to a reversible hydrogen electrode (RHE), by adding $(0.241 + 0.059$ pH) V. The *iR*-correction was manually performed on the basis of EIS results. The compensated potential was determined by $E_{compensated} = E_{measured} - i \times R_s$, and the $R_s$ was the series resistance determined by EIS.

The electrochemical surface area (ECSA) was used to quantify active-sites on electrocatalysts. However, the accurate ECSA cannot be determined directly, because of the unclear capacitive behavior. Alternatively, double-layer capacitance ($C_{dl}$) proportional to ECSA was employed, and it was derived from cyclic voltammograms (CVs) with various scan rates in a potential window without Faradaic currents. Then, the value of ECSA can be calculated with an assumed specific capacitance (SC) among 20–60 μF cm$_{ECSA}^{-2}$ for a flat surface. The formula is shown as follow:

$$S_{ECSA} = \frac{C_{dl} \times S_{GEO}}{SC}, \qquad SC = 20 \sim 60 \mu F\ cm_{ECSA}^{-2}$$

### 2.4. Density functional calculations

Density functional theory (DFT) calculations for selenide electrocatalysts were performed using the CASTEP module in Material Studio. Generalized gradient approximation (GGA) with Perdew-Burke-Ernzerhof (PBE) functional was used for the DFT exchange correlation energy, and 300 eV of kinetic energy cutoff was assigned to the plane-wave basis set. The self-consistent field (SCF) tolerance was $1 \times 10^{-6}$
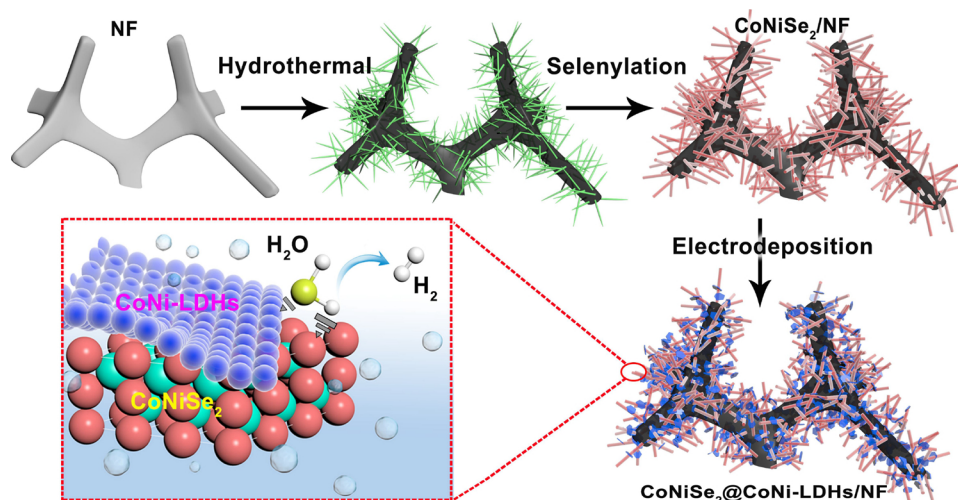
**Scheme 1.** Illustration for fabricating CoNiSe$_2$@CoNi-LDHs/NF composites.

eV, and the Brillouin zone was sampled by $1 \times 1 \times 1$ k-points. The core electrons were replaced with ultrasoft pseudo-potentials. To calculate adsorption energy, the CoNiSe$_2$(100) conjunct with Co-LDHs(003) or Ni-LDHs(003) were facets modeled, which were commonly observed crystalline facets. The Gibbs free-energy ($\Delta G_{H2O*}$) is described as:

$$\Delta G_{H2O*} = \Delta E_{H2O*} - T\Delta S$$

H$_2$O adsorption on electrocatalysts was performed by adding a H$_2$O molecule at a distance of 1.5 Å on the surface as initial structure for geometry optimization.

## 3. Results and discussion

### 3.1. Characterization of CoNiSe$_2$@CoNi-LDHs/NF

Featuring good mechanical strength, high electrical conductivity and rich porosity [29,30], commercial NF is utilized as a support and self-template to design selenide electrocatalysts with a 3D network. As displayed in Scheme 1, bimetallic CoNiSe$_2$ nanorods are fabricated via a hydrothermal selenidation of 1D Co-Ni precursor on NF (Fig. S1), and then surface-decorated by CoNi-LDHs via electrodeposition. In SEM observation (Fig. 1a), nanorods in the CoNiSe$_2$/NF are vertically attached on NF substrate. And TEM investigation reveals such nanorods consist of CoNiSe$_2$ (ICDD No. 01-070-2851) nanocrystals (Fig. 1b), agreeing with XRD analysis (Fig. S2). The characteristic lattice fringers of CoNiSe$_2$(101) and (102) are clearly observed. Meanwhile, EDS (Fig. S3) and the corresponding elemental mapping (Fig. 1c) confirm the uniform distribution of Ni, Co, and Se in the nanorods.

As displayed in Fig. 1d, the nanorods become thicker and rougher after CoNi-LDHs decoration via a fast electrodeposition process (2 min). TEM (inset of Fig. 1e) gives a clear proof for CoNiSe$_2$@CoNi-LDHs heterostructures that consist of nanorods hierarchically decorated by ultrathin nanosheets. The core nanorod presents the (010) and (100) lattice fringes of CoNiSe$_2$, while the surface nanosheets display the (015) of Ni(OH)$_2$·0.75H$_2$O (ICDD No. 01-038-0715). The visible defects (e.g., faultage, malposition and interface) imply rich active-sites for electrocatalysis. Moreover, EDS (Fig. S4) and elemental mapping (Fig. 1f) confirm the main elements of Ni, Co, Se, and O in such heteronanorods. Noticeably, the narrowed distribution of Se, in comparison with tubular O pattern, confirms a selenide core surface-decorated by LDHs.

Raman spectra and XPS were further conducted to investigate the above heterostructures. In Raman profiles (Fig. 2a), the CoNiSe$_2$@CoNi-LDHs/NF presents the bands associated with CoNiSe$_2$ (152, 186, 232 and 270 cm$^{-1}$) and CoNi-LDHs (457 and 522 cm$^{-1}$) [15], which are identical with those observed on CoNiSe$_2$ and CoNi-LDHs counterparts (Fig. S5). The bands at 372 and 481 cm$^{-1}$ are associated with Se species coupled with oxygen as exposed to air. Moreover, the XPS profiles of Co 2p and Ni 2p identify the consistent hybrid composition (Fig. 2b). In the Co 2p profile, the peaks at 779.0 and 793.7 eV can be ascribed to Co 2p$_{3/2}$ and 2p$_{1/2}$ in selenides, and a couple at 781.3 and 796.9 eV is assigned to Co$^{II}$ in LDHs [27]. They are accordingly observed on CoNiSe$_2$ and LDHs counterparts (Fig. S5). The similar situation is also presented by Ni 2p XPS, confirming the hybridization of CoNiSe$_2$ and LDHs. In addition, the Se 3d profile clearly shows the Se species bonded to Co and Ni, consistent with the bimetallic nature in selenides (Fig. S6).

### 3.2. HER performance

To evaluate HER activity, the CoNiSe$_2$@CoNi-LDHs/NF was tested in 1.0 M KOH employing a typical three-electrode configuration. For comparison, CoNiSe$_2$/NF, CoNi-LDHs/NF, bare NF, and commercial Pt/C on NF with similar mass loading were also tested. Fig. 3a displays the polarization curves after iR-drop corrections. The featureless polarization curve for bare NF guarantees a minimal background. The CoNiSe$_2$@CoNi-LDHs/NF affords high HER activity with a low $\eta_{10}$ of only 106 mV. It obviously outperforms the single-component counterparts of CoNi-LDHs/NF ($\eta_{10}$ = 264 mV) and CoNiSe$_2$/NF ($\eta_{10}$ = 192 mV), indicating the synergic enhancement between LDHs and CoNiSe$_2$. As compared with recently-reported selenide-based catalysts (Table S1), the CoNiSe$_2$@CoNi-LDHs/NF performs among the best. Its $\eta_{10}$ of 106 mV is lower than that of EG/Ni$_3$Se$_2$/Co$_9$S$_8$ (~150 mV) [31], NiFe LDH-NiSe/NF (~170 mV) [32], Co-Ni-B (133 mV) [33], NiSe$_2$@NiO$_x$ (132 mV) [24], CoSe$_2$/carbon cloth (130 mV) [34], and comparable to that of Ni$_{0.33}$Co$_{0.67}$Se$_2$/carbon fiber paper (106 mV) [20], and P-doped CoSe$_2$ (104 mV) [18].

Tafel plot and EIS analysis were further conducted to understand the electrocatalytic performance. In the Tafel plots (Fig. 3b), the CoNiSe$_2$@CoNi-LDHs/NF delivers an onset overpotential ($\eta_{onset}$) of 30 mV and a Tafel slope ($b$) of 74 mV dec$^{-1}$, lower than those of NF ($\eta_{onset}$ = 250 mV, $b$ = 149 mV dec$^{-1}$), CoNi-LDHs/NF ($\eta_{onset}$ = 160 mV, $b$ = 112 mV dec$^{-1}$), and CoNiSe$_2$/NF ($\eta_{onset}$ = 127 mV, $b$ = 98 mV dec$^{-1}$). The low Tafel slope on CoNiSe$_2$@CoNi-LDHs/NF indicates a quick increase in H$_2$ generation rate with applied overpotential, in accordance with its high activity in polarization curves (Fig. 3a). Typically, HER in alkaline aqueous media proceeds in two steps [35,36]. The first one is discharging H$_2$O (Volmer reaction, Eq. (1)) with a Tafel slope of 118 mV dec$^{-1}$, and the second one is either the H$_{ads}$ and H$_2$O reaction (Heyrovsky reaction, Eq. (2)) with a slope of 40 mV dec$^{-1}$, or the H$_{ads}$
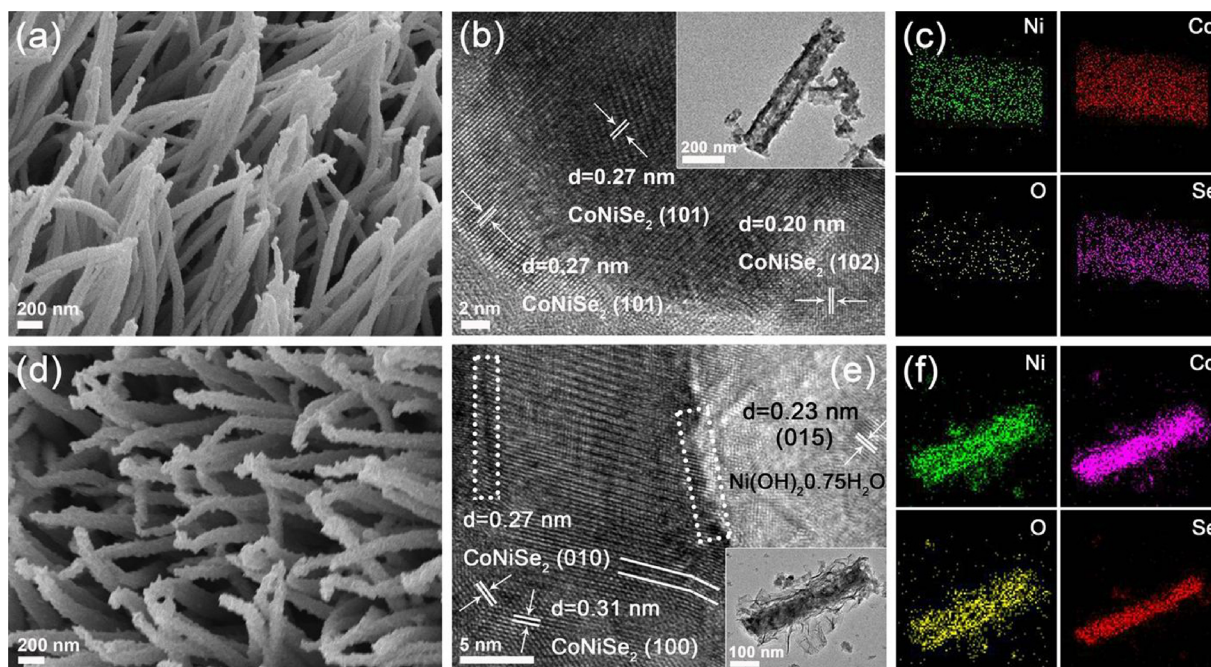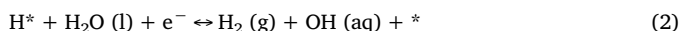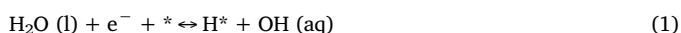
**Fig. 1.** (a, d) SEM and (b, e) TEM images, and (c, f) elemental mapping of (a–c) CoNiSe$_2$/NF and (d–f) CoNiSe$_2$@CoNi-LDHs/NF. In panel e, the defects (e.g., faultage, malposition, and interfaces) on CoNiSe$_2$@CoNi-LDHs are marked.

combination reaction (Tafel reaction, Eq. (3)) with a slope of 30 mV dec$^{-1}$. The Tafel slope on CoNiSe$_2$/NF as high as 98 mV dec$^{-1}$ indicates a rate-determination mostly by Volmer step, i.e., the discharge of H$_2$O to generate H$_{ads}$. The evidently reduced slope (74 mV dec$^{-1}$) on CoNiSe$_2$@CoNi-LDHs/NF suggests the facilitated Volmer step after LDHs decoration, and the rate-determined step turns to a transition between Volmer and Hyrovsky reactions [37]. Meanwhile, EIS profiles identify the lower charge-transfer resistance on CoNiSe$_2$@CoNi-LDHs/NF than that on CoNiSe$_2$/NF, CoNi-LDHs/NF and bare NF (Fig. 3c), which is associated with the promoted HER on heterostructures.

$$H_2O\ (l) + e^- + * \leftrightarrow H^* + OH\ (aq) \tag{1}$$

$$H^* + H_2O\ (l) + e^- \leftrightarrow H_2\ (g) + OH\ (aq) + * \tag{2}$$

$$H^* + H^* \leftrightarrow H_2\ (g) + 2* \tag{3}$$

The ECSA is a good way to quantify active-sites on electrocatalysts; however its accurate determination is difficult due to unclear capacitive behaviors. Herein, double-layer capacitances (C$_{dl}$) are alternatively measured as they are proportional to the ECSA [28]. Via plotting the current density variation in cyclic voltammograms (CVs, Fig. S7) versus scan rates, the C$_{dl}$ values can be estimated by the slopes of the fitting lines (Fig. 3d). The CoNiSe$_2$@CoNi-LDHs/NF presents a C$_{dl}$ of 106.4 m F cm$_{geo}$$^{-2}$, visibly higher than that of CoNiSe$_2$/NF (32.9 m F cm$_{geo}$$^{-2}$), CoNi-LDHs/NF (3.6 m F cm$_{geo}$$^{-2}$) and bare NF (2.6 m F cm$_{geo}$$^{-2}$). This indicates the remarkably enriched active-sites after LDHs decoration, owing to the hierarchical nanostructures evenly integrating 1D CoNiSe$_2$ with 2D CoNi-LDHs.

Generally, the specific capacitance for a flat surface (1 cm$^2$) is found to be in the range of 20–60 μF cm$^{-2}$ [38], and a moderated value of 40 μF cm$^{-2}$ is herein adopted to calculate the ECSA and make clear comparison. As indicated, the CoNiSe$_2$@CoNi-LDHs/NF gives a higher value of 186.2 cm$^2_{ECSA}$ than that of CoNiSe$_2$/NF (57.6 cm$^2_{ECSA}$). Subsequently, electrocatalytic currents normalized by ECSA ($j_{ECSA}$) can be used to inquire the specific HER activity [5]. As shown in Fig. 3e, the CoNiSe$_2$@CoNi-LDHs/NF affords a higher absolute $j_{ECSA}$ in comparison with CoNiSe$_2$/NF. At $\eta$ = 200 mV, the absolute $j_{ECSA}$ on the former (0.025 mA cm$_{ECSA}$$^{-2}$) is almost twice as high as that on the latter (0.015 mA cm$_{ECSA}$$^{-2}$), verifying the intrinsically improved activity on CoNi-LDHs decorated CoNiSe$_2$.

To interpret the high HER activity on CoNiSe$_2$@CoNi-LDHs heteronanorods, DFT calculations were conducted on CoNiSe$_2$(100) conjunct with Co-LDHs(003) or Ni-LDHs(003). After decoration by Co-



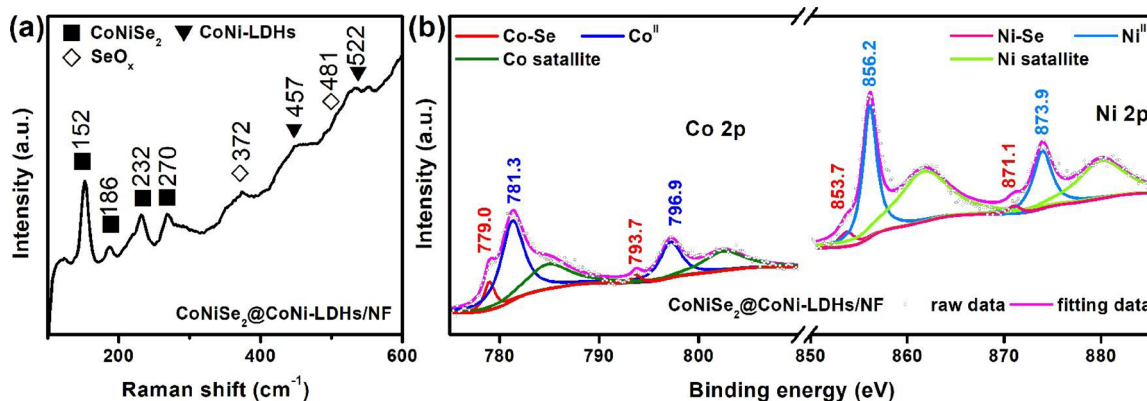**Fig. 2.** (a) Raman spectra of CoNiSe$_2$@CoNi-LDHs/NF, and (b) high-resolution XPS profiles of Co 2p and Ni 2p.
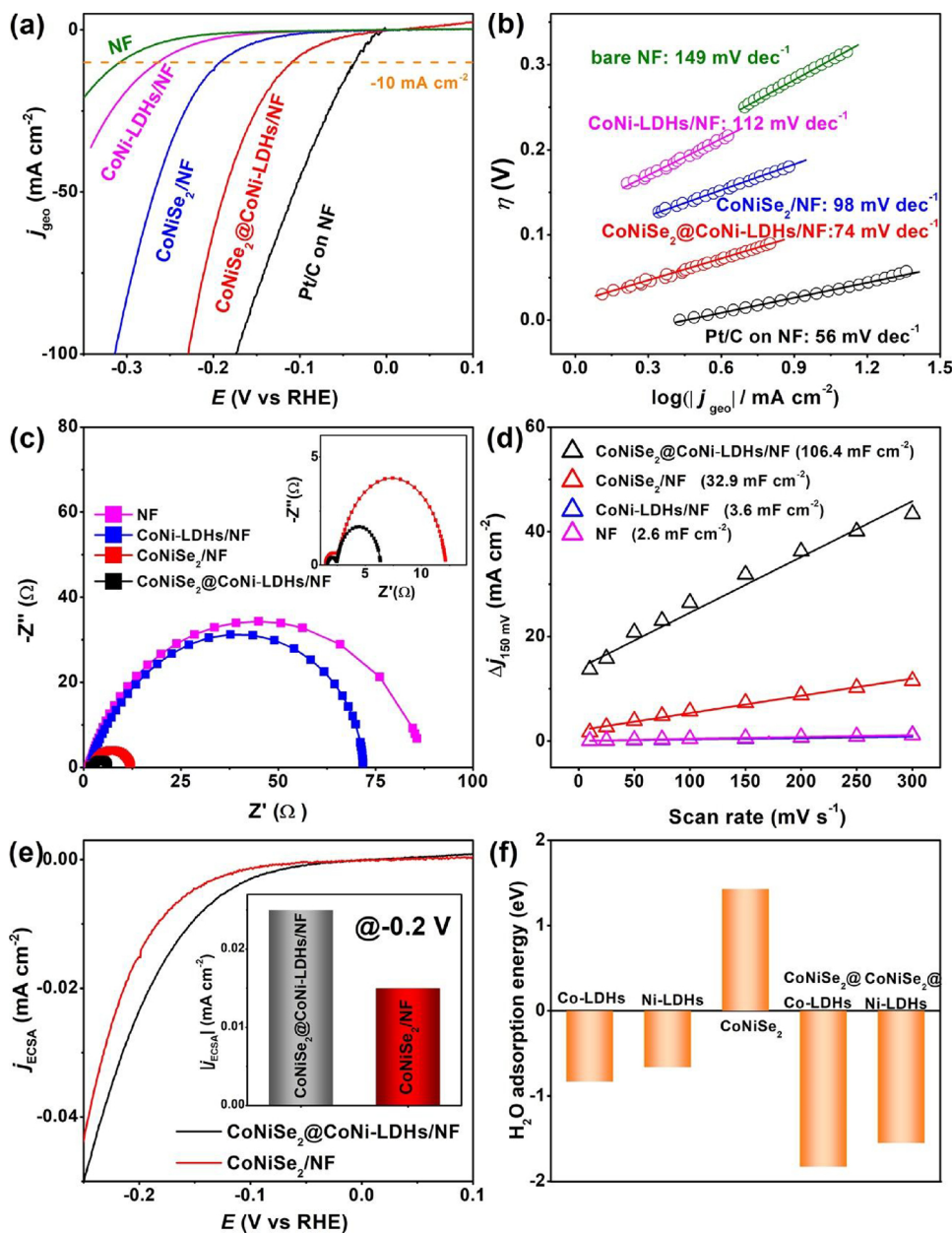
**Fig. 3.** (a) Polarization curves, (b) Tafel plots, (c) Nyquist plots (at $\eta$ = 200 mV), and (d) estimation of $C_{dl}$ by plotting the current density variation ($\Delta j = (j_a - j_c)/2$, at 150 mV vs. RHE; data obtained from the CVs in Fig. S7) of CoNiSe$_2$@Co-LDHs/NF and relevant counterparts in 1.0 M KOH. (e) $j_{ECSA}$ of CoNiSe$_2$/NF and CoNiSe$_2$@Co-LDHs/NF. (f) Gibbs free energy of H$_2$O adsorption on CoNiSe$_2$, CoNiSe$_2$@Co-LDHs and CoNiSe$_2$@Ni-LDHs. Insets of c and e present the magnificated EIS profiles and $j_{ECSA}$ at $-0.2$ V, respectively.

LDHs or Ni-LDHs, the reduced density of electronic states above the $E_F$ of CoNiSe$_2$ indicates strong electronic interactions (Fig. S8). Accordingly, the CoNiSe$_2$@Co-LDHs and CoNiSe$_2$@Ni-LDHs present a visibly downshifting d-band center of $-2.91$ and $-2.84$ eV, respectively, as compared with bare CoNiSe$_2$ ($-2.74$ eV). This hints electron transfer through CoNiSe$_2$-LDHs interfaces. In view of water dissociation as the key initial step in alkaline HER [19], H$_2$O chemisorption on the interface was further analyzed. The quite positive Gibbs free energy of H$_2$O adsorption (1.43 eV) on CoNiSe$_2$ suggests the unfavorable chemisorption (Fig. 3f). In sharp contrast, the surface decoration by Co- and Ni-LDHs obviously reduces the energy to $-1.83$ and $-1.55$ eV, indicating the favored chemisorption of polar H$_2$O on charge-redistributed interfaces. Subsequently, H$_2$O dissociation will be accelerated to produce H$_{ads}$ that is readily to react with H$_2$O toward H$_2$ evolution [39,40], leading to the intrinsically improved HER activity. Such promotion by LDHs decoration is also available in NiSe$_2$@LDHs/NF (Fig.

S9). However, its activity is still lower than that on bimetallic CoNiSe$_2$@CoNi-LDHs, associated with the inferior HER performance on NiSe$_2$. The solid-solution phase CoNiSe$_2$ with the regulated electronic configuration will favor the moderate binding with the H$_{ads}$ produced from water dissociation, leading to the fast turnover to gaseous H$_2$.

In this case, a balance between CoNiSe$_2$ and CoNi-LDHs is important to fulfil their synergy on interfaces. We thereby adopted different electrodeposition time to vary the interfacial structures. The SEM investigation clearly identifies that the LDHs decoration on CoNiSe$_2$ grows to large nanosheets with prolonged electrodeposition, and even covers the inner nanorods finally (Fig. S10). Accordingly, the increasing thickness of LDHs along with electrodeposition time is visible in TEM observation (Fig. S11). As evaluated for HER in 1.0 M KOH, the above composites deliver varied performance (Fig. 4a). Fig. 4b further summarizes the $\eta_{10}$ criterion of various CoNiSe$_2$@CoNi-LDHs/NF. Among them, the nanocomposites received via electrodeposition for 2 min
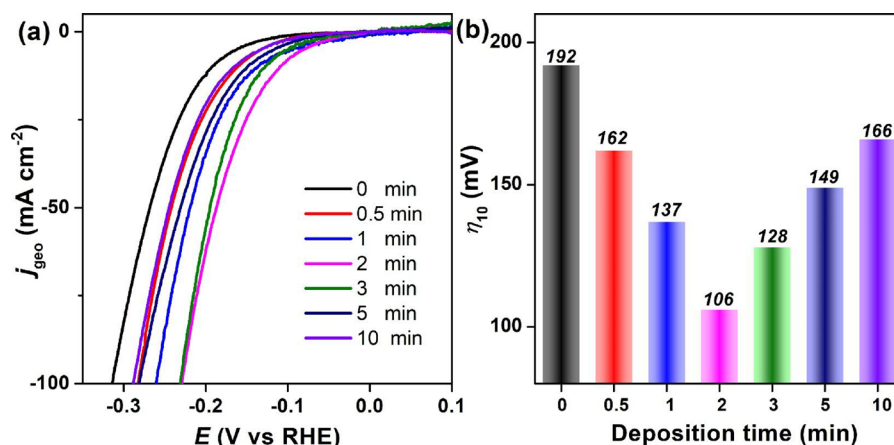
**Fig. 4.** (a) Polarization curves in 1.0 M KOH on a series of CoNiSe$_2$@CoNi-LDHs/NF obtained with different electro-deposition time, and (b) summary of the presenting $\eta_{10}$ values.

gives a lowest $\eta_{10}$ of 106 mV, indicating the optimal CoNiSe$_2$-LDHs heterointerfaces to balance fast water dissociation and consequent H$_{ads}$ desorption. As for short electrodeposition (e.g., 0.5 and 1 min), the LDHs decoration is inadequate on CoNiSe$_2$, resulting in weak interfacial synergy for HER. By contrast, the excessive LDHs decoration will obstruct the active-sites of selenides, and prohibit the further reduction of H$_{ads}$ toward H$_2$.

The long-term durability is another important criterion for electrocatalysts. Herein, 10,000 cycles are continuously tested in 1.0 M KOH (Fig. 5a), after which the CoNiSe$_2$@CoNi-LDHs/NF remains its high activity. However, slight deactivation is detectable. It suffers more 40 mV in the applied overpotential at $j_{geo} = -100$ mA cm$^{-2}$. The SEM observation presents the coarsened nanorods after test (inset of Fig. 5a), suggesting surface variations. We further carried out *in-situ* Raman investigation along with chronoamperometry test. The *j*-t curve at $\eta = 200$ mV shows a deterioration after 30 h (inset of Fig. 5b). The *in-situ* Raman spectra present the according structural variation (Fig. 5c). Although the bands associated with CoNiSe$_2$ (152, 189, 232 and 271 cm$^{-1}$) are well-remained during electrolysis, those assigned to Ni (Co)−OH (445 cm$^{-1}$) and Ni(Co)−O (532 cm$^{-1}$) fade away after 30 h, indicating the gradually removal of surface decoration by electrochemical milling. Such degradation of LDHs modification is responsible for the electrocatalysis deterioration, and more importantly points out the main contribution of their heterostructures to HER.

### 3.3. OER and overall water splitting

We further examined the OER performance in 1.0 M KOH. Fig. 6a displays the CV curves for CoNiSe$_2$@CoNi-LDHs/NF, CoNiSe$_2$/NF,

CoNi-LDHs/NF, and bare NF at a scan rate of 1.0 mV s$^{-1}$, along with that for IrO$_2$/C supported by NF with the same mass loading. It's visible that the anodic (1.36 V) and cathodic (1.26 V) peaks on CoNiSe$_2$@CoNi-LDHs/NF correspond to the redox reaction of surface Co and Ni species during OER [16], as suggested by XPS investigation (Fig. S12). Such reversible surface oxidation is important to *in-situ* generate active-sites for efficient OER [41,42]. However, the former disturbs the identification on $\eta_{10}$ in anodic scanning. Thereby, the cathodic scanning curves are taken into account when we discuss catalytic activity and the following Tafel plots. As expected, CoNiSe$_2$@CoNi-LDHs/NF delivers a high OER activity with quite low $\eta_{10}$ (208 mV) and $\eta_{100}$ (343 mV). It obviously outperforms the CoNi-LDHs/NF ($\eta_{10} = 314$ mV, $\eta_{100} = 382$ mV), but slightly the CoNiSe$_2$/NF ($\eta_{10} = 230$ mV, $\eta_{100} = 346$ mV). In comparison with the HER, the improvement in OER by LDHs decoration is not much obvious, especially in low-potential range. It should be noticed that OER is initiated from the oxidation of OH$^-$ [43], independent of water dissociation in an alkaline environment. Thus, the promotion by CoNi-LDHs in HER does not work in OER. In further comparison with benchmarking IrO$_2$/C (Fig. 6a) and recently reported noble-metal-free electrocatalysts (Table S2), our CoNiSe$_2$@CoNi-LDHs/NF still features its low overpotentials, suggesting its promise as cost-efficient substitutes for noble metals. Moreover, the Tafel plots verify the promoted kinetics on CoNiSe$_2$@CoNi-LDHs heteronanorods (Fig. 6b), in comparison with CoNiSe$_2$ and CoNi-LDHs counterparts. Coincident with the OER activity, CoNiSe$_2$@CoNi-LDHs/NF exhibits a $R_{ct}$ smaller than CoNiSe$_2$/NF and CoNi-LDHs/NF (Fig. S13), indicating the fast Faradaic process on heterostructures. In addition, the CoNiSe$_2$@CoNi-LDHs/NF can be stably operated for 48 h with a *j* of 25 mA cm$^{-2}$ at $\eta = 300$ mV, confirming the satisfied long-term
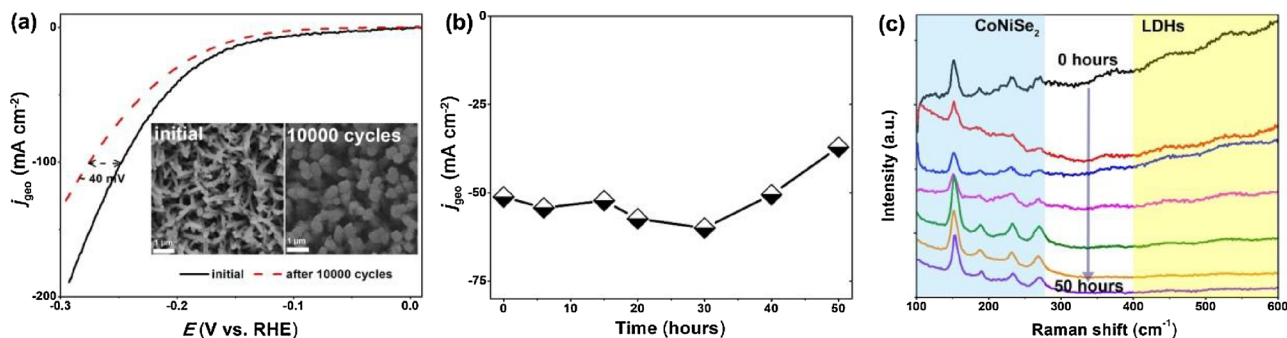


**Fig. 5.** (a) Polarization curves before and after 10,000 cycles, and (b) chronoamperometry curve of CoNiSe$_2$@CoNi-LDHs/NF in 1.0 M KOH, and (c) *in-situ* Raman corresponding with the chronoamperometry curve. (inset of a) SEM images of CoNiSe$_2$@CoNi-LDH/NF before and after 10,000 cycles.
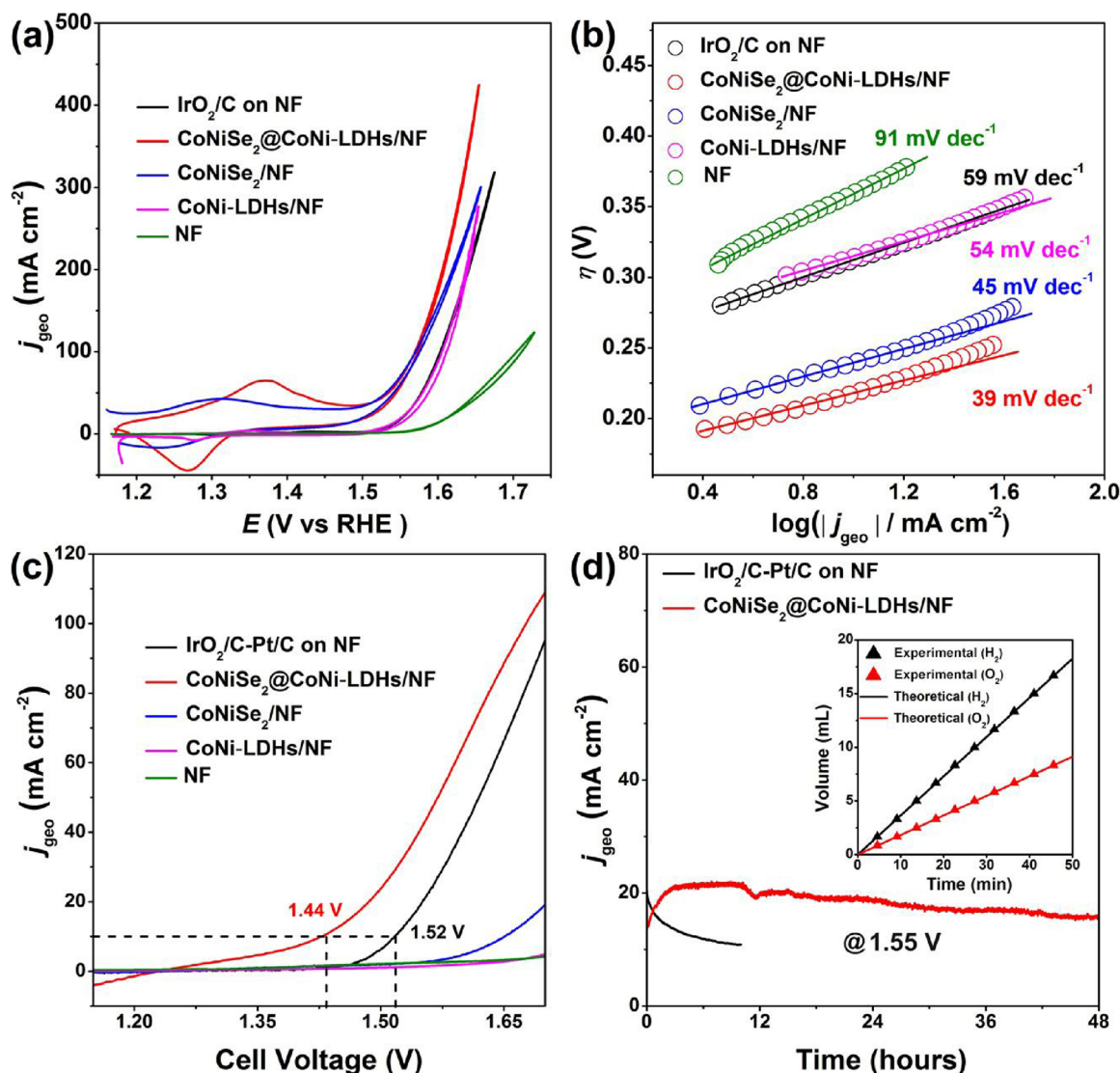
**Fig. 6.** (a) CV curves (scan rate: 1 mV s$^{-1}$) and (b) the corresponding Tafel plots of CoNiSe$_2$@Co-LDHs/NF and relevant counterparts in 1.0 M KOH. (c) Polarization curves, and (d) long-term durability tests at 1.55 V on CoNiSe$_2$@CoNi-LDHs/NF for overall water splitting in 1.0 M KOH. Inset of d shows the amount of gas theoretically calculated and experimentally measured versus time on CoNiSe$_2$@CoNi-LDHs/NF.

durability for OER (Fig. S14).

For a final electrolyzer device, CoNiSe$_2$@CoNi-LDHs/NF was integrated as both cathode and anode in a two-electrode system. They afford a superior activity for overall water splitting, with a cell voltage as low as 1.44 V to achieve a $j_{geo}$ of 10 mA cm$^{-2}$ (Fig. 6c). This performance is superior to that of CoNiSe$_2$/NF (1.65 V), CoNi-LDHs/NF (1.75 V), and even benchmarking IrO$_2$/C–Pt/C couple (1.52 V), indicating the compatible integration of HER and OER on CoNiSe$_2$@CoNi-LDHs/NF. It should be noted that both of CoNiSe$_2$@CoNi-LDHs/NF and CoNiSe$_2$/NF deliver similar OER activity, as implied by the $\eta_{10}$ of 208 and 232 mV, respectively. The tremendously reduced cell voltage for water electrolysis on CoNiSe$_2$@CoNi-LDHs/NF is reasonably ascribed to the improved HER after CoNi-LDHs decoration, highlighting the key role of HER in alkaline water electrolysis. In comparison with recently reported bi-functional electrocatalysts (Table S3), our CoNiSe$_2$-CoNi-LDHs/NF (1.44 V @ 10 mA cm$^{-2}$) outperforms NiFe LDHs-NiSe/NF (1.53 V) [32], NiCo-LDH/NF (1.66 V) [44], CoNiSe$_2$/NF (1.59 V) [45], Co-Ni-Se/C/NF (1.6 V) [46], Se-(NiCo)S$_x$/(OH)$_x$ nanosheets (1.6 V) [47], Co-doped NiSe$_2$/Ti mesh (1.62 V) [48], NiCo$_2$S$_4$/NF (1.63 V) [49], CoP/carbon cloth (1.65 V) [50], etc.

Moreover, such electrolyzer can be stably operated for 48 h,

affording a stable $j_{geo}$ of 20 mA cm$^{-2}$ at 1.55 V (Fig. 6d). Its long-term durability is obviously superior to IrO$_2$/C–Pt/C couple. In addition, the Faradaic efficiency for H$_2$ and O$_2$ evolution was analyzed. As shown in the inset of Fig. 6d, the amounts of H$_2$ and O$_2$ are experimentally quantified by gas chromatography versus time, which are in good accordance with the theoretical values. Such high-degree consistency confirms an efficiency approximate to 100%.

## 4. Conclusions

In summary, we have developed CoNiSe$_2$@CoNi-LDHs/NF heterostructures with excellent HER activity toward efficient water splitting. The promoted HER kinetics is experimentally and therotically evidenced on selenides-LDHs heterointerfaces, due to the enhanced H$_2$O chemisorption and dissociation to generate reactive H$_{ads}$. Thereby, the optimal nanocomposites afford a superior HER performance with a low $\eta_{10}$ of 106 mV in 1.0 M KOH. By contrast, such effect is negligible for OER. As for overall water splitting, the heteronanorods require a cell voltage of only 1.44 V at 10 mA cm$^{-2}$, outperforming most of noble-metal-free electrocatalysts and even IrO$_2$/C–Pt/C couple. Elucidating efficient electrocatalysis on engineered interfaces, this work will pave

the way for developing high-performance and cost-efficient electro-catalysts in energy chemistry.

## Appendix A. Supplementary data

Supplementary material related to this article can be found, in the online version, at doi:https://doi.org/10.1016/j.apcatb.2018.09.082.

## References

[1] T.R. Cook, D.K. Dogutan, S.Y. Reece, Y. Surendranath, T.S. Teets, D.G. Nocera, Chem. Rev. 110 (2010) 6474–6500.
[2] V. Di Noto, T.A. Zawodzinski, A.M. Herring, G.A. Giffin, E. Negro, S. Lavina, Int. J. Hydrogen Energy 37 (2012) 6120–6131.
[3] Z.W. Seh, J. Kibsgaard, C.F. Dickens, I. Chorkendorff, J.K. Nørskov, T.F. Jaramillo, Science 355 (2017) eaad4998.
[4] I. Roger, M.A. Shipman, M.D. Symes, Nat. Rev. Chem. 1 (2017) 0003.
[5] Q. Gao, W. Zhang, Z. Shi, L. Yang, Y. Tang, Adv. Mater. 30 (2018) 1802880.
[6] S.H. Ahn, B.-S. Lee, I. Choi, S.J. Yoo, H.-J. Kim, E. Cho, D. Henkensmeier, S.W. Nam, S.-K. Kim, J.H. Jang, Appl. Catal. B: Environ. 154 (2014) 197–205.
[7] R. Subbaraman, D. Tripkovic, D. Strmcnik, K.-C. Chang, M. Uchimura, A.P. Paulikas, V. Stamenkovic, N.M. Markovic, Science 334 (2011) 1256–1260.
[8] V.R. Stamenkovic, D. Strmcnik, P.P. Lopes, N.M. Markovic, Nat. Mater. 16 (2017) 57–69.
[9] H. Yin, S. Zhao, K. Zhao, A. Muqsit, H. Tang, L. Chang, H. Zhao, Y. Gao, Z. Tang, Nat. Commun. 6 (2015) 6430.
[10] R. Subbaraman, D. Tripkovic, K.-C. Chang, D. Strmcnik, A.P. Paulikas, P. Hirunsit, M. Chan, J. Greeley, V. Stamenkovic, N.M. Markovic, Nat. Mater. 11 (2012) 550–557.
[11] V.M. Nikolic, S.L. Maslovara, G.S. Tasic, T.P. Brdaric, P.Z. Lausevic, B.B. Radak, M.P.M. Kaninski, Appl. Catal. B: Environ. 179 (2015) 88–94.
[12] Y. Zhang, Q. Zhou, J. Zhu, Q. Yan, S.X. Dou, W. Sun, Adv. Funct. Mater. 27 (2017) 1702317.
[13] S. Anantharaj, S.R. Ede, K. Sakthikumar, K. Karthick, S. Mishra, S. Kundu, ACS Catal. 6 (2016) 8069–8097.
[14] A. Sivanantham, S. Shanmugam, Appl. Catal. B: Environ. 203 (2017) 485–493.
[15] F. Wang, Y. Li, T.A. Shifa, K. Liu, F. Wang, Z. Wang, P. Xu, Q. Wang, J. He, Angew. Chem. Int. Ed. 55 (2016) 6919–6924.
[16] C. Tang, N. Cheng, Z. Pu, W. Xing, X. Sun, Angew. Chem. Int. Ed. 54 (2015) 9351–9355.
[17] Q. Gong, L. Cheng, C. Liu, M. Zhang, Q. Feng, H. Ye, M. Zeng, L. Xie, Z. Liu, Y. Li, ACS Catal. 5 (2015) 2213–2219.
[18] Y.-R. Zheng, P. Wu, M.-R. Gao, X.-L. Zhang, F.-Y. Gao, H.-X. Ju, R. Wu, Q. Gao, R. You, W.-X. Huang, S.-J. Liu, S.-W. Hu, J. Zhu, Z. Li, S.-H. Yu, Nat. Commun. 9 (2018) 2533.
[19] B. Liu, Y.F. Zhao, H.Q. Peng, Z.Y. Zhang, C.K. Sit, M.F. Yuen, T.R. Zhang, C.S. Lee, W.J. Zhang, Adv. Mater. 29 (2017) 1606521.
[20] C. Xia, H. Liang, J. Zhu, U. Schwingenschlögl, H.N. Alshareef, Adv. Energy Mater. 7 (2017) 1602089.
[21] L. Najafi, S. Bellani, R. Oropesa-Nunez, A. Ansaldo, M. Prato, A.E.D.R. Castillo, F. Bonaccorso, Adv. Energy Mater. 8 (2018) 1703212.
[22] Y. Chen, Z. Ren, H. Fu, X. Zhang, G. Tian, H. Fu, Small 14 (2018) 1800763.
[23] Y. Liu, Q. Li, R. Si, G.-D. Li, W. Li, D.-P. Liu, D. Wang, L. Sun, Y. Zhang, X. Zou, Adv. Mater. 29 (2017) 1606200.
[24] H. Li, S. Chen, H. Lin, X. Xu, H. Yang, L. Song, X. Wang, Small 13 (2017) 1701487.
[25] J. Hu, C. Zhang, L. Jiang, H. Lin, Y. An, D. Zhou, M.K.H. Leung, S. Yang, Joule 1 (2017) 383–393.
[26] E. Jung, H.-Y. Park, A. Cho, J.H. Jang, H.S. Park, T. Yu, Appl. Catal. B: Environ. 225 (2018) 238–242.
[27] C. Xia, Q. Jiang, C. Zhao, M.N. Hedhili, H.N. Alshareef, Adv. Mater. 28 (2016) 77–85.
[28] Y. Yang, K. Zhang, H. Lin, X. Li, H.C. Chan, L. Yang, Q. Gao, ACS Catal. 7 (2017) 2357–2366.
[29] J. Zhao, X. Li, G. Cui, X. Sun, Chem. Commun. 54 (2018) 5462–5465.
[30] X. Ji, R. Zhang, X. Shi, A.M. Asiri, B. Zheng, X. Sun, Nanoscale 10 (2018) 7941–7945.
[31] Y. Hou, M. Qiu, G. Nam, M.G. Kim, T. Zhang, K. Liu, X. Zhuang, J. Cho, C. Yuan, X. Feng, Nano Lett. 17 (2017) 4202–4209.
[32] S. Dutta, A. Indra, Y. Feng, T. Song, U. Paik, ACS Appl. Mater. Interfaces 9 (2017) 33766–33774.
[33] S. Gupta, N. Patel, R. Fernandes, R. Kadrekar, A. Dashora, A.K. Yadav, D. Bhattacharyya, S.N. Jha, A. Miotello, D.C. Kothari, Appl. Catal. B: Environ. 192 (2016) 126–133.
[34] Q. Liu, J. Shi, J. Hu, A.M. Asiri, Y. Luo, X. Sun, ACS Appl. Mater. Interfaces 7 (2015) 3877–3881.
[35] S. Jing, L. Zhang, L. Luo, J. Lu, S. Yin, P.K. Shen, P. Tsiakaras, Appl. Catal. B: Environ. 224 (2018) 533–540.
[36] P. Ganesan, A. Sivanantham, S. Shanmugam, J. Mater. Chem. A 4 (2016) 16394–16402.
[37] T. Shinagawa, A.T. Garcia-Esparza, K. Takanabe, Sci. Rep. 5 (2015) 13801.
[38] C. Zhang, Y. Huang, Y. Yu, J. Zhang, S. Zhuo, B. Zhang, Chem. Sci. 8 (2017) 2769–2775.
[39] G. Yilmaz, K.M. Yam, C. Zhang, H.J. Fan, G.W. Ho, Adv. Mater. 29 (2017) 1606814.
[40] P. Chen, T. Zhou, M. Zhang, Y. Tong, C. Zhong, N. Zhang, L. Zhang, C. Wu, Y. Xie, Adv. Mater. 29 (2017) 1701584.
[41] M.W. Louie, A.T. Bell, J. Am. Chem. Soc. 135 (2013) 12329–12337.
[42] M. Lee, H.-S. Oh, M.K. Cho, J.-P. Ahn, Y.J. Hwang, B.K. Min, Appl. Catal. B: Environ. 233 (2018) 130–135.
[43] N.-T. Suen, S.-F. Hung, Q. Quan, N. Zhang, Y.-J. Xu, H.M. Chen, Chem. Soc. Rev. 46 (2017) 337–365.
[44] W. Liu, J. Bao, M. Guan, Y. Zhao, J. Lian, J. Qiu, L. Xu, Y. Huang, J. Qian, H. Li, Dalton Trans. 46 (2017) 8372–8376.
[45] T. Chen, Y. Tan, Nano Res. 11 (2018) 1331–1344.
[46] F. Ming, H. Liang, H. Shi, X. Xu, G. Mei, Z. Wang, J. Mater. Chem. A 4 (2016) 15148–15155.
[47] C. Hu, L. Zhang, Z.-J. Zhao, A. Li, X. Chang, J. Gong, Adv. Mater. 30 (2018) 1705538.
[48] T. Liu, A.M. Asiri, X. Sun, Nanoscale 8 (2016) 3911–3915.
[49] A. Sivanantham, P. Ganesan, S. Shanmugam, Adv. Funct. Mater. 26 (2016) 4661–4672.
[50] T. Liu, L. Xie, J. Yang, R. Kong, G. Du, A.M. Asiri, X. Sun, L. Chen, ChemElectroChem 4 (2017) 1840–1845.